

Band gap engineering in AA-stacked bilayer graphene

Hasan M. Abdullah,^{1,2,3,*} Mohammed Al Ezzi,^{4,†} and H. Bahloul^{1,2}

¹*Department of Physics, King Fahd University of Petroleum and Minerals, 31261 Dhahran, Saudi Arabia*

²*Saudi Center for Theoretical Physics, P.O. Box 32741, Jeddah 21438, Saudi Arabia*

³*Department of Physics, College of Applied Science, Taiz University, Yemen*

⁴*Department of Physics, National University of Singapore, 2 Science Drive 3, Singapore 117551, Singapore*

(Dated: August 29, 2018)

We demonstrate that AA-stacked bilayer graphene (AA-BLG) encapsulated by dielectric materials can possess an energy gap due to the induced mass term. Using the four-band continuum model, we evaluate transmission and reflection probabilities along with the respective conductances. Considering interlayer mass-term difference opens a gap in the energy spectrum and also couples the two Dirac cones. This cone coupling induces an inter-cone transport that is asymmetric with respect to the normal incidence in the presence of asymmetric mass-term. The energy spectrum of the gapped AA-BLG exhibits electron-hole asymmetry that is reflected in the associated intra- and inter-cone channels. We also find that even though Klein tunneling exists in gated and biased AA-BLG, it is precluded by the interlayer mass-term difference and instead Fabry-Pérot resonances appear.

PACS numbers:

I. INTRODUCTION

The experimental realization of single graphene layers in 2004¹ have triggered tremendous interest in this material and its multilayer. The promising electrical, optical, mechanical properties as well as the great potential for sensor technology make graphene and its derivatives promising candidates for nanoscale device applications.^{2–4} Graphene's extraordinary properties make it a promising candidate for nanoscale device applications in the future. Moreover, bilayer graphene exists in two different types of stacking, namely, AB-(Bernal) and AA stackings (AB-BLG and AA-BLG). The stability of AB-BLG made it the subject of considerable investigations, both theoretical and experimental^{5–7}. On the contrary to the previous belief that AA-BLG samples are unstable, recent stable samples were realized^{8–11}. The linear gapless energy spectrum of pristine AA-BLG attracted considerable theoretical interest^{12–17}. Among the existing studies on AA-BLG are spin Hall effect^{18,19}, doping effects²⁰, dynamical conductivity²¹, tunneling through electrostatic and magnetic barriers^{22,23}, magnon transport²⁴, influence of spin orbit coupling on the band structure²⁵, and Landau levels in biased AA-BLG in the presence of nonuniform magnetic field²⁶.

The Klein tunnelling of Dirac fermions prevents the complete confinement in graphene. Overcoming this drawback can be achieved by opening a band gap in the energy spectrum by, for example, using slow Li⁺ ions or perpendicular electric field in single-layer graphene and AB-BLG, respectively^{5,27–29}. A different route to achieve a perfect confinement in single layer graphene was through graphene quantum blisters³⁰ where the charge carriers are confined on a delaminated bilayer graphene. In addition, substrates can also play a key role in the electronic confinement of single layer graphene due to the substrate-induced band gap of order of $\sim (20 - 500)$

meV^{31–37}. The width of the band gap depends on the mass term induced by the substrate whose magnitude can be in the order of $\sim (50 - 100)$ meV depending on the type of the substrate³⁸. It has been recently showed that Hall phase can be realized in gapped AB-BLG when mass terms are considered in both layers³⁹. Such mass terms are induced by dielectric materials such as hexagonal boron nitride (h-BN) or SiC.

A toy model suggested that a gap can be opened in AA-BLG if different spin-orbit coupling (SOC) are considered in each layer⁴⁰. However, controlling the SOC in each layer is practically not feasible and most importantly the SOC in graphene is considered extremely small which remains to be verified experimentally. For example, the gap induced by SOC is 0.8×10^{-5} meV for π orbit and 9.0 meV for the σ orbit²⁵. Another study showed that a band-gap in the transmission spectrum of AA-BLG with double magnetic barriers which can be tuned by a bias²².

In the present work we propose a configuration of AA-BLG that hosts a band gap in the energy spectrum arising from the dielectric-induced mass terms. Considering the same mass terms in both layers of AA-BLG opens a gap around the lower and upper cones whereas the whole spectrum remains gapless. On the other hand, considering different mass terms in both layers breaks the inversion symmetry and, hence, induces a gap in the energy spectrum. The width of the gap is directly affected by the inter-layer mass-term difference. Biasing the two layers of AA-BLG allows inter-cone transition due to the coupling of the upper and lower cones established by the bias. Such transition is forbidden in the case of zero bias but it can be also induced when different mass terms are considered in both layers.

This paper is organized as follows. In Sec. II, we present the model of our study and describe the different transition processes allowed in the system. Sec. III is devoted to numerical results and discussion of conduc-

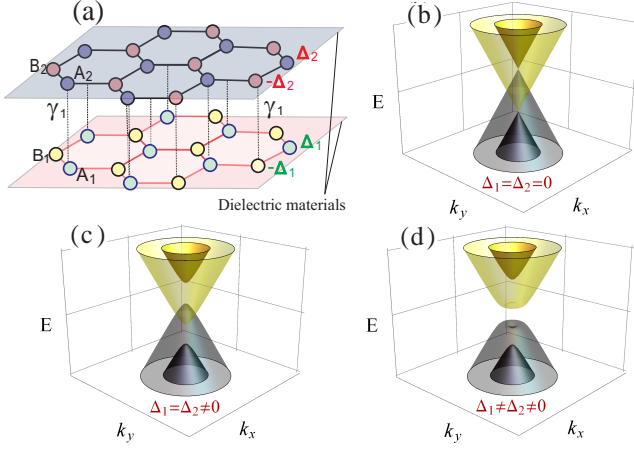


FIG. 1: (a) Crystalline structure of the AA-stacked graphene bilayer associated with the energy spectrum for: (b) zero mass-term amplitude, (c) same mass-term in both layers, and (d) with different mass terms which induces a gap in the spectrum.

tance, transmission and reflection probabilities. Finally, we conclude by stressing our main findings in Sec. IV.

II. ELECTRONIC MODEL AND ENERGY SPECTRUM

Single layer graphene has a hexagonal crystal structure comprising two atoms A and B in its unit cell whose interatomic distance $a = 0.142$ nm and inter-layer coupling $\gamma_0 = 3$ eV⁴¹. In the AA-stacked graphene bilayer the two single layer graphene are placed exactly on top of each other such that atoms A_2 and B_2 in the top layer are located directly above the atoms A_1 and B_1 in the bottom layer, with direct inter-layer coupling $\gamma_1 \approx 0.2$ eV⁴², see Fig. 1(a). The energy spectrum of AA-BLG for different amplitudes of the mass terms is shown in Figs. 1(b-d) where a gap arises as a result of interlayer mass-term difference. The presence of the gap in this case is

a manifestation of breaking the inversion symmetry. In AA-BLG all atoms take part in the interlayer coupling contrary to the AB-BLG where only half of the atoms participate and as a consequence $\gamma_1^{AB} = 2\gamma_1^{AA} \approx 0.4$ eV^{43–45}. Another difference is that the latter has asymmetric interlayer coupling, in other words, atom A_1 coupled to atom B_2 while the coupling is symmetric in the AA-BLG. Such differences give rise to the distinct band structure and transport properties in both types of stackings. The continuum approximation of the Hamiltonian which describes the electrons near one of the Dirac points K or K' of AA-BLG taking into account SOC and mass terms reads²¹

$$H^\tau = \begin{bmatrix} H_1^\tau & \gamma_1 I \\ \gamma_1 I & H_2^\tau \end{bmatrix}, \quad (1)$$

where $H_i^\tau = \tau v_F (p_x \sigma_x + \tau p_y \sigma_y) + \tau \sigma_z (s_z \lambda_i + \Delta_i) + V_i I$ is the single layer graphene Hamiltonian with V_i the electrostatic potential, whose width is d , on the i -th layer which can be varied using top and back gates on the sample and $v_F = 10^6$ m/s the charge carries speed in the graphene sheet, $p_{x,y} = -i\hbar\partial_{x,y}$, $\sigma_{x,y}$ and I are the 2×2 Pauli and identity matrices, respectively. The strength of the intrinsic SOC and the mass term, in the i -th layer are represented by λ_i and Δ_i , respectively, $\tau = \pm 1$ corresponds to the K and K' valleys and $s_z = \pm 1$ stands for the electron spin up and spin down. When considering only spin up $s_z = 1$ it becomes clear that the mass term plays exactly the same role as the SOC in the single layer Hamiltonian. Being extremely small, SOC has insignificant effect on the band structure and transport properties specially at high energies therefore it will be neglected in the further calculations of transmission, reflection and conductance. A simplification can be made to the Hamiltonian, in the vicinity of K valley, by applying unitary transformation that forms symmetric and anti-symmetric combination of the top and bottom layers. This results in a Hamiltonian in the basis $\Psi = 2^{-1/2}(\Psi_{A2} + \Psi_{A1}, \Psi_{B2} + \Psi_{B1}, \Psi_{A2} - \Psi_{A1}, \Psi_{B2} - \Psi_{B1})^T$ of the form:

$$H = \begin{pmatrix} \gamma_1 + v_0 + \Delta_0 & v_F \pi^\dagger & \delta + \Omega & 0 \\ v_F \pi & \gamma_1 + v_0 - \Delta_0 & 0 & \delta - \Omega \\ \delta + \Omega & 0 & -\gamma_1 + v_0 + \Delta_0 & v_F \pi^\dagger \\ 0 & \delta - \Omega & v_F \pi & -\gamma_1 + v_0 - \Delta_0 \end{pmatrix}. \quad (2)$$

where $v_0 = (V_2 + V_1)/2$, $\delta = (V_2 - V_1)/2$, $\Delta_0 = (\Delta_2 + \Delta_1)/2$, and $\Omega = (\Delta_2 - \Delta_1)/2$. Introducing the length scale $l = \hbar v_F / \gamma_1$, which represents the inter-layer

coupling length $l \approx 3.3$ nm, allows us to define the following dimensionless quantities:

$$E \rightarrow \frac{E}{\gamma_1}, v_0 \rightarrow \frac{v_0}{\gamma_1}, \delta \rightarrow \frac{\delta}{\gamma_1}, \Delta_0 \rightarrow \frac{\Delta_0}{\gamma_1}, \Omega \rightarrow \frac{\Omega}{\gamma_1}, k_y \rightarrow lk_y, \text{ and } \mathbf{r} \rightarrow \frac{\mathbf{r}}{l}.$$

As a result of the translational invariance along the y direction, the momentum in that direction is a conserved quantity and, hence, the wavefunction in the new basis can be written as

$$\Psi(x, y) = e^{iyk_y} [\phi_1, \phi_2, \phi_3, \phi_4]^\dagger, \quad (3)$$

where \dagger stands for the transpose. Implementing Schrodinger equation $H\Psi = E\Psi$ leads to four coupled differential equations:

$$-i \left[\frac{d}{dx} + ky \right] \phi_2 + (\delta + \Omega) \phi_3 = (\epsilon - 1 - \Delta_0) \phi_1 \quad (4)$$

$$-i \left[\frac{d}{dx} - ky \right] \phi_1 + (\delta - \Omega) \phi_4 = (\epsilon - 1 + \Delta_0) \phi_2 \quad (5)$$

$$-i \left[\frac{d}{dx} + ky \right] \phi_4 + (\delta + \Omega) \phi_1 = (\epsilon + 1 - \Delta_0) \phi_3 \quad (6)$$

$$-i \left[\frac{d}{dx} - ky \right] \phi_3 + (\delta - \Omega) \phi_2 = (\epsilon + 1 + \Delta_0) \phi_4 \quad (7)$$

where $\epsilon = E - v_0$. The system of coupled first-order differential equations (4-7) can be transformed into a single second order differential equation for ϕ_2 as follows

$$\left[\frac{d^2}{dx^2} + (k_x^\pm)^2 \right] \phi_2 = 0, \quad (8)$$

where

$$k_x^\pm = \left[-k_y^2 + \beta^2 \pm \sqrt{\xi^2 + 4(\epsilon^2 - \Omega^2)} \right]^{1/2}, \quad (9)$$

with $\beta^2 = 1 + \epsilon^2 + \delta^2 - \Delta_0^2 - \Omega^2$ and $\xi = 2(\epsilon\delta + \Delta_0\Omega)$. From Eq. (9), it follows that the energy spectrum for the system is given by

$$\epsilon_\alpha^\pm = \frac{1}{2} \left[\alpha\sigma \pm \sqrt{-(\sigma^2 + 2\rho) - 2\text{sgn}(\alpha)\frac{\kappa}{\sigma}} \right]^{1/2}, \quad (10)$$

where $\alpha = \pm 1$ and σ, ρ , and κ functions are defined in Appendix A. In Fig. 2, we show the energy spectra of the AA-BLG for different values of the system parameters. For $\delta = 0$, the characterized quantities ΔE , Δk_y , ΔE_m , and E_g in Fig. 2 are defined as follows

$$\Delta E = 2 \left| \sqrt{1 + \Omega^2} - \Delta_0 \right|, \quad (11a)$$

$$\Delta k_y = 2\sqrt{1 - \Delta_0^2(1 + \Omega^2)}, \quad (11b)$$

$$\Delta E_m = 2\Delta_0, \quad (11c)$$

$$E_g = 2\sqrt{(1 - \Delta_0^2)|\Omega|}. \quad (11d)$$

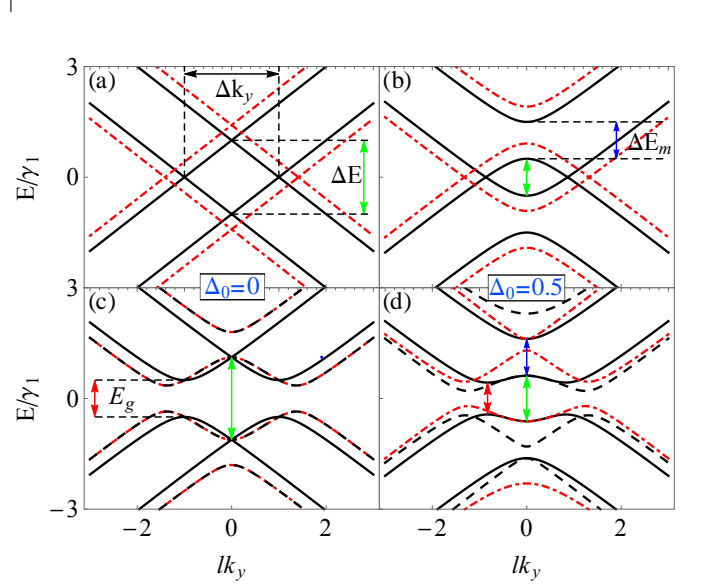


FIG. 2: Energy spectrum of AA-stacked bilayer graphene with (a) no mass term been considered, (b) the same mass terms in both layers, (c) different mass terms in top and bottom layers, and (d) same magnitude and different sign in each layer (solid black curves). The dashed orange and black curves correspond to the same system but with electric fields in opposite directions with $\delta = (1, -1)\gamma_1$, respectively.

AA-BLG has a linear energy spectrum with two up-down Dirac cones shifted by ΔE , which is $2\gamma_1$ in this case as shown in Fig. 2(a) by the solid black curves. When AA-BLG is subjected to a perpendicular electric field (biased AA-BLG) the two Dirac cones are slightly shifted and situated at $v_0 \pm \sqrt{\gamma_1^2 + \delta^2}$, see dotted-dashed orange curves in Fig. 2(a). Fig. 2(b) is the same as Fig. 2(a) but with the same mass term amplitude $\Delta_0 = 0.5\gamma_1$ for both layers and the spectrum exhibits a shift ΔE_m in the bands around the upper and lower Dirac cones. Introducing a mass term difference $\Omega = 0.5\gamma_1$ with mass term amplitude $\Delta_0 = 0.5\gamma_1$ leads to opening a gap E_g in the energy spectrum as shown in Fig. 2(c) where solid black, dotted-dashed orange, and dashed black curves correspond to $\delta = (0, 1, -1)\gamma_1$, respectively. Notice that considering biased AA-BLG ($|\delta| \neq 0$) with inter-layer mass-term difference and non-zero amplitude, i.e. $(\Omega, \Delta_0) \neq 0$, breaks the electron-hole symmetry as indicated by the black dashed and dotted-dashed orange curves in Fig. 2(d). The energy spectrum exhibits another symmetry which can be obtained under the exchange $[E(k_y), -\delta] \leftrightarrow [-E(k_y), \delta]$. In contrast, keeping the mass-term difference $\Omega = 0.5\gamma_1$ but with zero amplitude $\Delta_0 = 0$ restores the electron-hole symmetry under the exchange $\delta \leftrightarrow -\delta$ without affecting the existence of

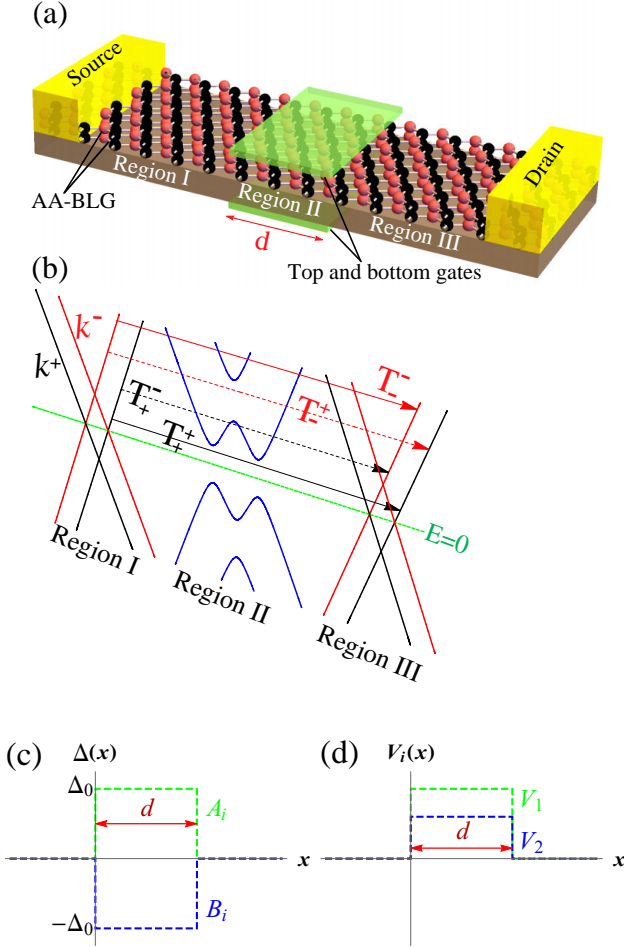


FIG. 3: (a) Schematic representation of the proposed system with the parameters of the electrostatic rectangular potential on each layer of AA-BLG. (b) The mass term profile on sublattices A_i and B_i in the i -th layer. (c) Electrostatic potential strength V_i applied to the i -th layer.

the energy gap E_g , see Fig. 2(c).

A. Transitions probabilities

To investigate the quantum transport of the proposed system in Fig. 3(a), we first need to find the wavefunction in each region, see Appendix B for more details. In the first I ($x < 0$) and third III ($x > d$) regions we have pristine AA-BLG. While in the intermediate region II ($0 < x < d$) the mass term induced by the dielectric materials as well as electrostatic potential is included. The induced mass-term on sublattices A_i and B_i has the same amplitude but different sign as shown in Fig. 3(c), while the electrostatic potentials applied to top and bottom layers have the same effect on both sublattices, see Fig. 3(d). In AA-BLG, there are two propagating modes for all energies in contrast to AB-BLG whose two modes only exist for energies exceeding the interlayer coupling. These two modes k^+ and k^- exist outside the interac-

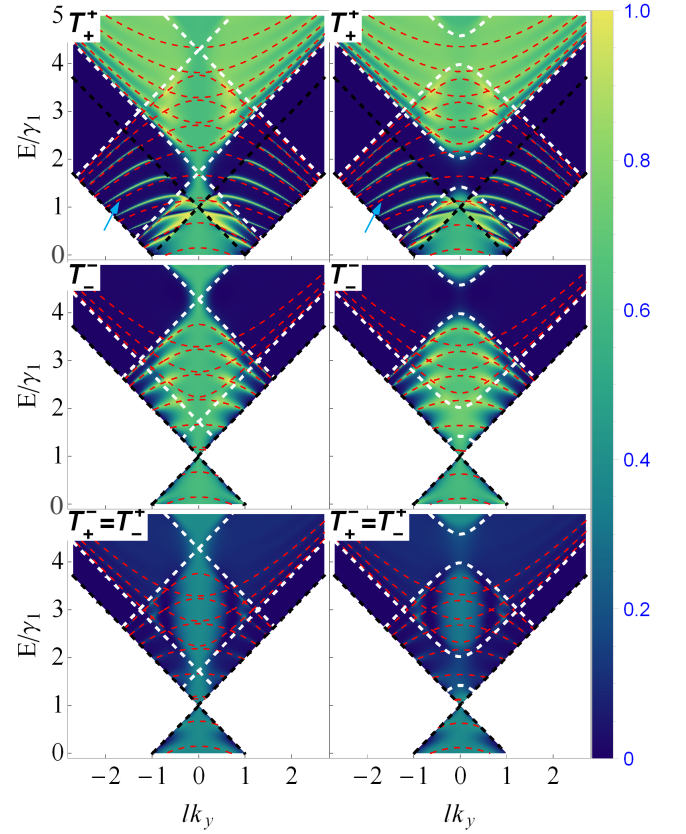


FIG. 4: Density plot of the transmission probabilities for $\Omega = 0$, $v_0 = 3\gamma_1$, $d = 6l$, $\delta = 0.8\gamma_1$, with $\Delta_0 = 0$ (left panel) and $\Delta_0 = 0.3\gamma_1$ (right panel). The superimposed dashed black and white curves correspond to the bands outside and inside the barrier regions, respectively. The red dashed curves correspond to the Fabry-Pérot resonances given by Eq. (14).

tion region III and correspond to the lower and upper Dirac cones, respectively, see Fig. 3(b). Hence, we need to consider the different transition probabilities between the lower and upper cones. There are four different transmission probabilities as illustrated in Fig. 3(b). We label a transition from one cone to another by A_i^j which denotes a charge carrier scattering from the cone k^i to the cone k^j , where A can stand for transmission (T) or reflection (R) probabilities with $i, j = \pm$. In Appendix B we explain how to obtain these probabilities. The diagonal blocks of the Hamiltonian in Eq.(3) represents two cones shifted in energy by $2\gamma_1$ (for $\Delta_0 = 0$) while the off-diagonal blocks characterize the coupling strength between the two cones. Therefore, for $\Omega = \delta = 0$ the Hamiltonian stands for two decoupled cones where scattering between them is strictly forbidden. The scattering between these two cones can be induced only by the electrostatic potential bias δ or the interlayer mass-term difference Ω . The different processes of the inter- or intra-transition between the lower and upper cones are shown in Fig. 3(b). Consequently, considering the scattering process between the two cones results in four channels

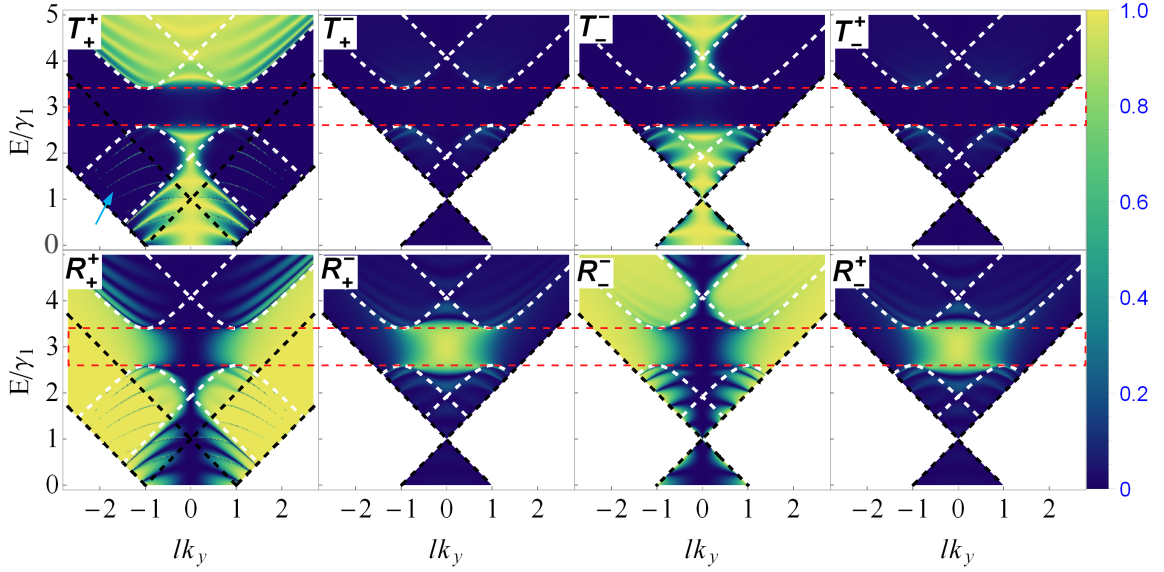


FIG. 5: Density plot of the transmission and reflection probabilities for $\Omega = 0.4\gamma_1$, $v_0 = 3\gamma_1$, $d = 6l$, $\delta = 0$, with $\Delta_0 = 0$. The superimposed dashed black and white curves correspond to the bands outside and inside the barrier regions, respectively.

for the transmission T_{\pm}^j as well as for the reflection R_{\pm}^j probabilities. For normalization consideration we have

$$\sum_{j=\pm} (T_{\pm}^j + R_{\pm}^j) = 1. \quad (12)$$

For example, for the lower cone we have $T_+^+ + R_+^+ + T_+^- + R_+^- = 1$. The zero temperature conductance can be calculated using the Büttiker's formula^{46,47}

$$G_i^j(E) = G_0 \frac{L_y}{2\pi} \int_{-\infty}^{+\infty} dk_y T_i^j(E, k_y), \quad (13)$$

with $(i, j) = \pm$, L_y the length of the sample in the y -direction, and $G_0 = 4e^2/h$. The factor 4 comes from the valley and spin degeneracy in graphene. The total conductance of the system is the sum through all available channels $G_T = \sum_{i,j} G_i^j$.

III. NUMERICAL RESULTS AND DISCUSSION

As discussed in the preceding sections, scattering between the lower and upper cones can be induced only

by inter-layer bias or inter-layer mass difference. The effect of the mass-term amplitude on the transport properties and Klein tunneling in unbiased⁴⁸ and biased⁴⁹ AA-BLG has been studied before. Here we briefly discuss the results of a biased AA-BLG in the presence of the mass-term amplitude to compare the strength of inter-cone scattering with the one arisen by the interlayer mass-term difference. In Fig. 4 we show the density plot of the different transmission channels as a function of the Fermi energy and the wave vector k_y for $\Delta_0 = 0$ ($0.3\gamma_1$ in left (right) panel). We notice that the presence of the mass-term amplitude completely suppresses the intra-cone transmission (T_+^+ and T_-^-) in the vicinity of the upper and lower cones ($v_0 - (+)\gamma_1 + \Delta_0 \geq E \geq v_0 - (+)\gamma_1 - \Delta_0$) as depicted in Fig. 4 (right panel). On the other hand, the profile of the inter-cone transmission ($T_-^+ = T_+^-$) shows finite transport within the same energy ranges rendering charge carriers in the system unconfined⁴⁹. The propagating modes interfere with themselves in the interaction region as a result of the finite size effect. This interference leads to oscillation in the transmission probabilities at quantized energies. For $\Omega = 0$ this so-called Feby-Pérot resonances⁴⁶ appear at

$$E_{\alpha,n}^{\pm}(k_y) = v_0 + \alpha \sqrt{1 + k_y^2 + \delta^2 + \Delta_0^2 + \left(\frac{n\pi}{d}\right)^2} \pm \sqrt{(1 + \delta^2) \left(k_y^2 + \Delta_0^2 + \left(\frac{n\pi}{d}\right)^2\right)}, \quad (14)$$

where $\alpha = \pm 1$. These energies are superimposed as

red dashed curves in Fig. 4. The resonances given by

Eq. 14 are valid only when the modes inside and outside the barrier are propagating as can be inferred from the intra- and inter-cone channels T_+^+ and T_-^- . For example, the resonances marked by the blue arrow in the channel T_+^+ in Fig. 4 do not obey Eq. 14. Such resonances occur in regions where the k^+ mode inside the barrier is evanescent while it is propagating outside. They are arising as a result of the cones coupling established by the bias, see Eq. 2, and they completely vanish once the two cone are decoupled⁴⁹.

So far, we have assumed that the interlayer mass-term difference is zero in the interaction region. To thoroughly examine its effect on the intra- and inter-cone transport, we show in Fig. 5 the corresponding transmission and reflection probabilities in the presence of a symmetric mass-term amplitude, i.e. $\Delta_0 = 0$ while $\Omega = 0.4\gamma_1$. The different probabilities are plotted as a function of the conserved wave vector k_y and the Fermi energy E . The white zone in Fig. 5 indicates the absence of the relevant propagating mode in the incident region which coincides with evanescent waves. At first glance, we note that all intra- and inter-cone channels in transmission and reflection are invariant under $k_y \rightarrow -k_y$ rendering it symmetric with respect to normal incidence. This is a manifestation of the symmetric mass term introduced on both layers as well as the symmetric inter-layer coupling in AA-BLG. These symmetries also result in a symmetric inter-cone transport such that $T_+^- = T_-^+$ and $R_+^- = R_-^+$ as can be inferred from Fig. 5. Due to the absence of the propagating modes in the interaction region that are indispensable for tunneling, the intra- and inter-cone transmission have been completely suppressed within the induced gap, i.e. in the range $v_0 + E_g/2 \geq E \geq v_0 - E_g/2$, with $E_g = 0.8\gamma_1$ as expressed in Eq. (11d). Furthermore, we notice also that the major transmitted current is carried out through the intra-cone channel T_+^+ . This implies that the cone coupling established by mass-term difference is weak compared to the one induced by the potential bias. The coupling effect can be also seen in the fringes within the domain marked by the blue arrow in the T_+^+ channel. They are attenuated and sharper than those in Fig. 4. On the other hand, we find that the reflection profiles display a slightly different features as clarified in Fig. 5. Of particular significance is the remarkable observation of the extremely strong inter-cone reflection R_i^j within the energy gap, specially near the normal incidence direction. In addition, for normal incidence the inter-cone reflection is finite, contrary to the inter-cone transmission which is strictly zero. This is a consequence of the fact that the inversion and chiral symmetries are broken in the presence of the interlayer mass-term difference.

As an illustration of the mass-term influence on chiral tunnelling properties and the cone coupling, we show the transmission as a function of the wave vector k_y and the width of the interaction region d in Figs. 6(b, d), respectively. It is also instructive to compare it with the case of biased AA-BLG to elucidate the effect of bias and to give a deeper understanding of the cone coupling, as depicted

in Fig. 6(a, c). First we consider the cone coupling established by the potential and mass-term difference and show the inter-cone transmission in Figs. 6(a, b), respectively, for different Fermi energies. Fig. 6(a) shows the inter-cone transmission induced as a result of the cone coupling established by the interlayer potential bias. We note that with increasing the Fermi energy of the incident charge carriers, the strength of the associated maxima is invariable. Thus, it is clear that this maximum does not depend on the incident Fermi energy but rather on the bias strength and the width of the interaction region as will be clarified latter. On the other hand, from Fig. 6(b) one can see that for normal incidence the inter-cone transmission induced by the interlayer mass-term difference is strictly zero. It is significant around the edges of the gap and vanishes at low or high energies. The fact that at normal incidence the inter-cone transmission is finite and zero with interlayer bias and mass-term difference, respectively, can be attributed to the chiral symmetry in the system. Introducing a bias dose not break the chiral symmetry in the system, but it is broken in the case of the interlayer mass-term difference. This suggests that the Klein tunneling should hold in the presence of the electrostatic bias and disappear with introducing the interlayer mass difference.

To elucidate how the Klein tunneling would be affected by the bias and the interlayer mass-term difference, we show in Figs. 6(c, d) the intra- and inter-cone transmission and reflection for normal incidence as a function of the interaction region width d . Before proceeding, we would like to remind the readers that we have two channels corresponding to the lower and upper cones. Each channel is normalized to unity and thus to observe Klein tunneling the total transmission and reflection of each channel must be unity and zero, respectively. Fig. 6(c) shows all channels in case of finite bias and zero mass-term difference. It reveals that the intra- T_i^i and inter-cone T_i^j transmissions oscillate in anti-phase with increasing the width of the interaction region, while both intra- and inter-cone reflections are zero. The maxima associated with intra- and inter-cone transmission coincide with the width

$$d_n = \frac{\pi(n + \eta)}{\sqrt{1 + \delta^2}} \quad (15)$$

with $n = 0, 1, 2, \dots$, and $\eta = (0, 1/2)$ for T_i^i and T_i^j , respectively. Such oscillation was also observed within domain walls in delaminated bilayer graphene⁷. Note that the location of these maxima is independent of the Fermi energy. Moreover, we can clearly now see that $T_i^i + T_i^j = 1$ and $R_i^i + R_i^j = 0$ regardless of the width of the interaction region d . This is a quintessential trait of Klein tunneling in the system. Consequently, the system retains Klein tunneling even in the presence of the potential bias. On the contrary, in the presence of the interlayer mass-term difference the intra-cone transmission T_i^i and inter-cone reflection R_i^j are finite while T_i^j and R_i^i vanish, see Fig. 6(d). Again, we see also here that the none zero channels

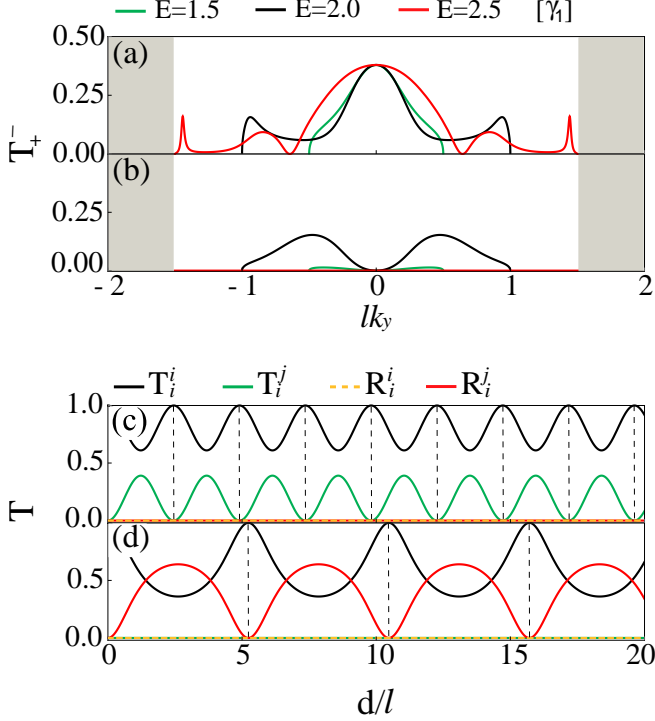


FIG. 6: (a, b) Inter-cone transmission as a function of the transverse wave vector k_y at different energies with $d = 6l$, $v_0 = 3\gamma_1$, $\Delta_0 = 0$. We consider only potential bias in panel (a), i.e. $\delta = 0.8\gamma_1$, $\Omega = 0$, and interlayer mass-term difference in panel (b), i.e. $\delta = 0$, $\Omega = 0.8\gamma_1$. The gray zones in panel (a) indicate the absence of the relevant propagating mode in the incident region. (c, d) Intra- and inter-cone channels for normal incidence as a function of interaction region width d , the parameters are set the same as in panels (a, b), respectively.

T^i and R^j oscillate in anti-phase but with a large period compared to the previous case with the bias. The location of the resonances in T^i (coincide with $R^j=0$) are given by

$$d_n = \frac{\pi n}{\sqrt{|(E - v_0)^2 - \Omega^2|}}. \quad (16)$$

Note that these locations are energy dependent in contrast to those in the biased system shown in Fig. 6(c). For example, in the energy interval $0 < E < v_0 - \Omega$, as the energy increases, fewer resonances appear in the considered interaction width. Most importantly, we observe that $T^i + T^j \neq 1$ and $R^i + R^j \neq 0$ are always preserved unless $d = d_n$. In other words, the backscattering is not strictly prohibited as the case when Klein tunneling exists, but instead a non-zero reflected current exists at specific widths. Hence, we conclude that in the presence of the interlayer mass-term difference Klein tunneling is hampered, and instead Fabry-Pérot resonances appear.

Next, we consider asymmetric mass-term on both layers such that $\Delta_0 = 0.3\gamma_1$ and $\Omega = 0.4\gamma_1$ and show all

possible transmission and reflection channels in Fig. 7. The most remarkable feature is the asymmetric inter-cone transmission with respect to normal incidence such that $T^+(k_y) = T^+(-k_y)$. This asymmetry feature is also strongly pronounced within the gap in all reflection channels. However, the inter-cone reflections are the same such that $R^+(k_y) = R^+(-k_y)$ since the carriers are reflected to the same region of incidence. This angular asymmetry manifests that the Hamiltonian in Eq. (2) is not invariant under the exchange $k_y \rightarrow -k_y$ and in the presence of Ω and Δ_0 . Note that breaking only the interlayer symmetry in AA-BLG by considering either $\delta \neq 0$ or $\Omega \neq 0$ leaves the Hamiltonian in Eq. (2) invariant under the exchange $k_y \rightarrow -k_y$, and thus results in symmetric transmission and reflection probabilities, see Figs. (4, 5). For example, for $\delta \neq 0$ we can show that $H(k_y) = UH(-k_y)$ where U here is a unitary transformation corresponding to an interchange of the ϕ_1 and ϕ_2 basis together with $\phi_3 \leftrightarrow \phi_4$. This is diametrically opposite to the AB-BLG⁵⁰ system where breaking the interlayer symmetry destroys such invariance under the exchange $k_y \rightarrow -k_y$. This discrepancy stems from the symmetric and asymmetric interlayer coupling in AA-BLG and AB-BLG systems, respectively. Furthermore, comparing Fig. 7 with the results in Fig. 5, we see that here channels carry out a non-zero current for normal incidence which is an extra consequence of breaking the angular symmetry. It is important to point out that in the vicinity of the other valley, the inter-cone transmission is given by $T^j(k_y)_K = T^j(-k_y)_{K'}$. This angular asymmetry; however, leaves the valley degeneracy unchanged and thus the overall symmetry of the system is preserved as well as the macroscopic time reversal symmetry. Eventually, it is worth to mention that the cloaking effect presents in gapless⁵¹ and gapped⁵⁰ AB-BLG is absent in AA-BLG as can be deduced from Figs. (5, 7).

In Fig. 8, we plot the variation of the inter- and intra-cone transmission probabilities, for normal incidence, in terms of the potential bias δ and Fermi Energy E for zero and finite mass-term amplitude Δ_0 . When looking at the transmission profiles, one can distinguish two kinds of symmetry, namely, cone and electron-hole symmetries. In the cone symmetry, the two intra-cones transmission are connected through $T^+_+(E, \delta) = T^+_-(-E, \tau\delta)$ with $\tau = (+, -)$ for $\Delta_0 = 0$ and $\Delta_0 \neq 0$, respectively. While the electron-hole symmetry is only preserved in the inter-cone transmission such that $T^+_+(E, -\delta) = T^+_-(-E, \delta)$.

As a measurable quantity, we show in Fig. 9 the intra-, inter-cone and total conductances of the system. In all panels we consider an electrostatic potential of strength $v_0 = 3\gamma_1$ whose width is $d = 6l$ and the rest of parameters δ, Δ_0 , and Ω are varied. In all panels, we note that the total conductance is considerably large for $E = 0$ in striking contrast to single layer graphene⁵² and AB-BLG⁵³. This originates from the availability of propagating states at $E = 0$ corresponding to lower and upper cones in AA-BLG, as attested by the plots of Fig. 2(a). In single layer graphene and AB-BLG, such prop-

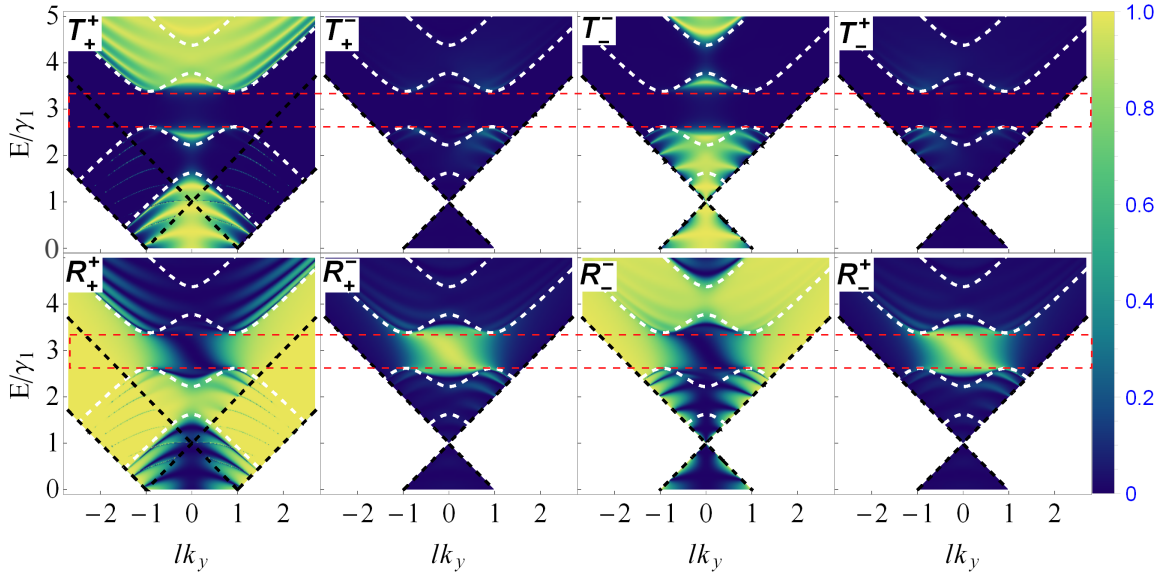


FIG. 7: Density plot of the transmission and reflection probabilities for $\Omega = 0.4\gamma_1$, $v_0 = 3\gamma_1$, $d = 6l$, $\delta = 0$, with $\Delta_0 = 0.3\gamma_1$. The superimposed dashed black and white curves respectively correspond to the bands outside and inside the barrier regions.

agating states are absent at $E = 0$ and only through evanescent states a ballistic transport takes place⁴⁶. The overall conductance profiles in Figs. 9(a, b) exhibit smoothed resonances, particularly for $E < v_0$, inherited from the transmission resonances. For example, at low energy the intra-cone channel T_-^- possesses resonances of flat shape⁴⁹ that appear as sharp peaks in the conductance. These peaks correspond to energy situated almost at the tail of the resonances in the channel T_-^- . Since the tail of the resonances coincide with $\pm\pi/2$ angle of incidence, we can calculate the peak energies using Eq. (14) where it can be rewritten for $\delta = 0$ as $E_n = 1 + \sec^2 \phi \left(v_0 - \sqrt{v_0^2 \sin^2 \phi + \kappa^2 \cos^2 \phi} \right)$, with ϕ is the incident angle and $\kappa^2 = [\Delta_0^2 + (n\pi/d)^2]$. Now, we can see that for $\phi \rightarrow \pm\pi/2$, $E_7 = (0.261, 0.246)\gamma_1$ for $\Delta_0 = (0, 0.3)\gamma_1$, respectively. These two peaks are superimposed as vertical dashed-blue lines in Figs. 9(a, b). Even though the total conductance profile G_T remains almost unaffected with or without the mass-term amplitude, as can be inferred from Figs. 9(a, b), the intra-cone conductances G_+^+ and G_-^- are drastically altered in the presence of mass term amplitude Δ_0 . In particular, they are totally suppressed in the vicinity of the lower and upper cones as clarified by the dashed-black and -blue curves in Fig. 9(b) and stipulated by the energy spectrum in Fig. 2(b). Note that the inter-cone conductance G_i^j is strictly zero as the two cones are being decoupled, see dashed-green curves in Figs. 9(a, b).

As shown in Figs. 9(c, d), the potential bias strongly modifies the positions and shapes of the resonances in the conductance channels. Of particular importance, it switches on the inter-cone conductance ($G_i^j \neq 0$), which in turn increases the total conductance and results in

pronounced resonances.

In panels (e, f) of Fig. 9, we show the conductance for finite interlayer mass-term difference with zero potential bias. The conductance profiles are almost similar to those in panels (a, b), respectively, but are influenced by the suppression in the energy range of the band gap at $E = v_0 \pm E_g/2$. Since the inter-cone conductance G_i^j is relatively small, the resonances in the energy interval $v_0 - E_g/2 > E > \gamma_1$ are smeared. Furthermore, we note that the total conductance is considerably large at the edges of the gap. From an applied perspective, this provides an efficient configuration to *switch on/off* the current through the sample using only an electrostatic gate. The presence of the gap also provides a characteristic signature of interlayer-mass term difference, which we expect to be elegantly observable in experiments. According to the total conductance profiles in panels (e, f), we note that within the gap the total conductance is not strictly zero. This is because we consider a relatively narrow interaction region, $d = 6l$, and thus evanescent waves can take part in the electronic transport⁴⁶. However, for $d \geq 10l$ the total conductance within the gap becomes completely zero.

IV. SUMMARY AND CONCLUSION

In conclusion, we proposed a configuration to establish a gap in the energy spectrum of AA-BLG by considering dielectric-induced mass term. We analytically derive the energy spectrum and the wavefunction of the system with symmetric and asymmetric mass term and in the presence of an electrostatic bias. We have evaluated the quantum transport through the biased and gapped

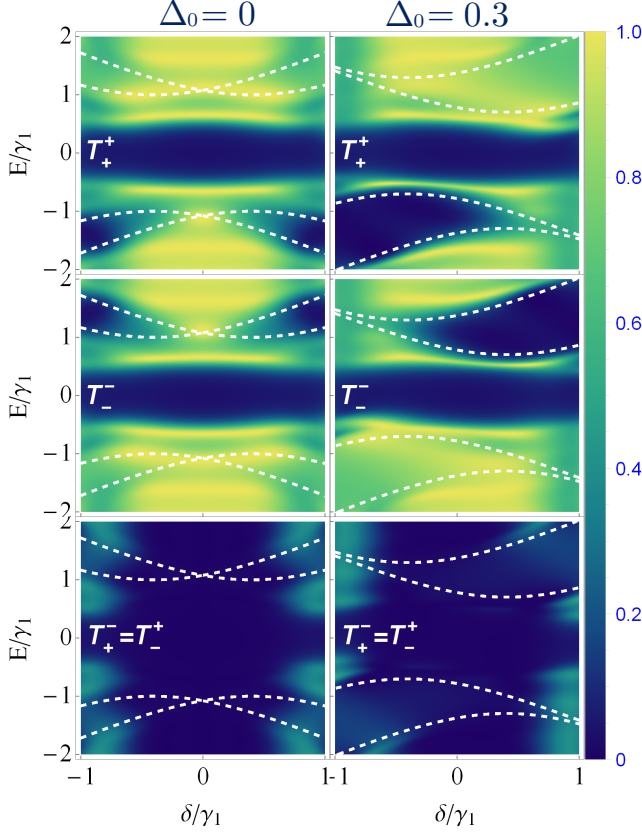


FIG. 8: Density plot of transmission probabilities of different channels as a function of the bias for $k_y = 0$, $\Omega = 0.4\gamma_1$, $v_0 = 0$, $d = 6l$. Positive and negative strengths of the bias correspond to electric field with opposite directions, the bands are superimposed as white dashed curves.

AA-BLG system. Specifically, we scrutinized chiral tunnelling properties of the charge carriers in the presence of the potential bias and interlayer mass-term difference. We found that Klein tunneling was maintained with the bias but the mass-term difference completely destroyed it and instead Febrý-Pérot resonances were surfaced. Furthermore, we showed that both parameters breaks the interlayer symmetry and couple the two Dirac cones. This coupling established inter-cone scattering that is asymmetric with respect to normal incidence when considering asymmetric mass term on both layers. In gapped AA-BLG, the electron-hole symmetry was broken and new symmetries emerged with the intra- and inter-cone channels, namely, $T_+^+(E, \delta) = T_-^-(-E, \tau\delta)$ and $T_+^-(E, -\delta) = T_-^+(-E, \tau\delta)$ with $\tau = (+, -)$ for $\Delta_0 = 0$ and $\Delta_0 \neq 0$.

For gated AA-BLG ($v_0 \neq 0$), we showed that the mass term amplitude Δ_0 slightly alters the total conductance while drastically changes the intra-cone conductances where they drop to zero in the vicinity of the upper and lower cones. On the other hand, the resulting conductance significantly increases in biased AA-BLG as

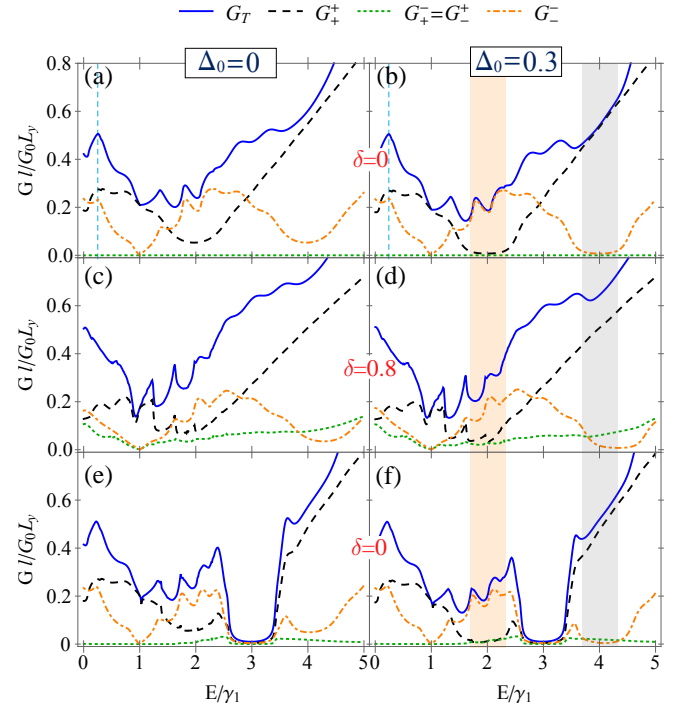


FIG. 9: Contribution of intra- and inter-cone conductances for $d = 6l$, $v_0 = 3\gamma_1$ with (a-d) $\Omega = 0$, and (e, f) $\Omega = 0.4\gamma_1$. The pink and gray regions in the right panels represent the gap width in the vicinity of lower and upper Dirac cones, respectively, which induced by the mass-term amplitude Δ_0 .

a result of the extra inter-cone channels that can be accessed by the bias. Consequently, the peaks in the total conductance become very pronounced and their locations are modified. Introducing the mass-term difference forms a distinct characteristic in the conductance represented by a gap whose location can be modulated by the electrostatic gate v_0 . Finally, we expect that the existence of topological states within the gap in this system is of great potential when considering a kink mass-term profile since they were already observed in single layer graphene^{37,54} whose spectrum resembles the one of AA-BLG. The results presented here are potentially exploitable for paving the way for electrical control of quantum transport in AA-BLG-based electronic devices.

Acknowledgment

We acknowledge the support of King Fahd University of Petroleum and Minerals under research group project RG171007-1 & RG171007-2. We also acknowledge the material support of the Saudi Center for Theoretical Physics (SCTP).

Appendices

Appendix A: Energy spectrum

The energy spectrum of the system can be obtained from Eq. (9) which gives

$$\epsilon_{\alpha}^{\pm} = \frac{1}{2} \left[\alpha \sigma \pm \sqrt{-(\sigma^2 + 2\rho) - \operatorname{sgn}(\alpha) \frac{2\kappa}{\sigma}} \right]^{1/2}, \quad (\text{A1})$$

where $\alpha = \pm 1$ and

$$\begin{aligned} \sigma &= \sqrt{\frac{1}{3} \left(-2\rho + \frac{C_0}{Q} + Q \right)}, \\ Q &= \frac{1}{2^{1/3}} \left(C_1 + \sqrt{C_1^2 - 4C_0^3} \right)^{1/3}, \\ \rho &= 2 \left[\eta^2 - 2(\delta^2 + 1) \right], \quad \kappa = 8\Omega\delta\Delta_0, \end{aligned}$$

with

$$\begin{aligned} C_0 &= \rho^2 + 12 \left[\eta^2 - 4\Omega^2(\Delta^2 - 1) \right], \\ C_1 &= 2\rho^3 + 27\kappa^2 - 72\rho \left[\eta^2 - 4\Omega^2(\Delta^2 - 1) \right], \\ \eta^2 &= 1 + \delta^2 - k_y^2 - \Delta_0^2 - \Omega^2. \end{aligned}$$

Appendix B: Wavefunction

The solution of Eq. (8) is a plane wave given by

$$\phi_2 = e^{ik_+x} + e^{-ik_+x} + e^{ik_-x} + e^{-ik_-x}. \quad (\text{B1})$$

Substituting this into equations (4-7) yields the solutions. The wave function of the system can be written in

matrix form as

$$\Psi(x, y) = GM(x)C e^{ik_y y}, \quad (\text{B2})$$

where the four-component vector C represents the different coefficients expressing the relative weights of the different traveling modes, which have to be set according to the propagating region⁵⁰. The matrices $M(x)$ and G are given by

$$M(x) = \text{Diag}[e^{ik_+x}, e^{-ik_+x}, e^{ik_-x}, e^{-ik_-x}], \quad (\text{B3})$$

and

$$G = \begin{pmatrix} \chi_+^- & \chi_+^+ & \chi_-^- & \chi_-^+ \\ 1 & 1 & 1 & 1 \\ \zeta_+^- & \zeta_+^+ & \zeta_-^- & \zeta_-^+ \\ \Lambda^+ & \Lambda^+ & \Lambda^- & \Lambda^- \end{pmatrix}, \quad (\text{B4})$$

where

$$\begin{aligned} \Lambda^{\pm} &= \frac{1 - k_y^2 - k_{\pm}^2 + -2(\epsilon + \Omega) + (\delta + \epsilon)^2 - \lambda^2}{2\sqrt{2}(\epsilon + \Omega)}, \\ \chi_{\alpha}^{\pm} &= \pm \frac{(k_{\alpha} \pm ik_y) [\sqrt{2}(\epsilon - \Delta_0) + \Lambda^{\alpha}(\mu + 1)]}{1 + (\delta + \Omega)^2 - (\Delta_0 - \epsilon)^2}, \\ \zeta_{\alpha}^{\pm} &= \pm \frac{(k_{\alpha} \pm ik_y) [\sqrt{2}(\Omega + \delta) + \Lambda^{\alpha}(\mu - 1)]}{1 + (\delta + \Omega)^2 - (\Delta_0 - \epsilon)^2}, \end{aligned}$$

with $\alpha = \pm$, $\lambda = \Delta_0 - \Omega$, and $\mu = \delta - \lambda - \epsilon$. Note that the above solution corresponds to the intermediate region *II* shown in Fig. 3(a). To obtain the desired solutions in regions *I* and *III* we need just to set $\delta = v_0 = \Delta_0 = \Omega = 0$ in the above equations. Then, implementing the transfer matrix together with appropriate boundary conditions gives the transmission and reflection probabilities^{50,55,56}.

* Electronic address: alshehab211@gmail.com

† Electronic address: alezzi@u.nus.edu

¹ A. K. Geim and K. S. Novoselov, Nat. Mater. **6**, 183 (2007).

² A. H. C. Neto, F. Guinea, N. M. R. Peres, K. S. Novoselov, and A. K. Geim, Rev. Mod. Phys. **81**, 109 (2009).

³ G. R. Berdiyrov, H. Abdullah, M. A. Ezzi, G. V. Rakhmatullaeva, H. Bahloul, and N. Tit, AIP Advances **6**, 125102 (2016).

⁴ N. Tit, M. M. A. Ezzi, H. M. Abdullah, M. Yusupov, S. Kouser, H. Bahloul, and Z. H. Yamani, Mater. Chem. Phys. **186**, 353 (2017).

⁵ T. Ohta, A. Bostwick, T. Seyller, K. Horn, and E. Rotenberg, Science **313**, 951 (2006).

⁶ M. O. Goerbig, Rev. Mod. Phys. **83**, 1193 (2011).

⁷ H. M. Abdullah, M. Zarenia, H. Bahloul, F. M. Peeters, and B. Van Duppen, Europhys. Lett. **113**, 17006 (2016).

⁸ J.-K. Lee, S.-C. Lee, J.-P. Ahn, S.-C. Kim, J. I. B. Wilson, and P. John, J. Chem. Phys. **129**, 234709 (2008).

⁹ J. Borysiuk, J. Sołtys, and J. Piechota, J. Appl. Phys. **109**,

093523 (2011).

¹⁰ P. L. de Andres, R. Ramírez, and J. A. Vergés, Phys. Rev. B **77**, 045403 (2008).

¹¹ Z. Liu, K. Suenaga, P. J. F. Harris, and S. Iijima, Phys. Rev. Lett. **102**, 015501 (2009).

¹² A. L. Rakhmanov, A. V. Rozhkov, A. O. Sboyachkov, and F. Nori, Phys. Rev. Lett. **109**, 206801 (2012).

¹³ Y. Mohammadi and B. A. Nia, Solid State Commun. **201**, 76 (2015).

¹⁴ R.-B. Chen, Y.-H. Chiu, and M.-F. Lin, Carbon **54**, 268 (2013).

¹⁵ C.-W. Chiu, S.-C. Chen, Y.-C. Huang, F.-L. Shyu, and M.-F. Lin, Appl. Phys. Lett. **103**, 041907 (2013).

¹⁶ A. Rozhkov, G. Giavaras, Y. P. Bliokh, V. Freilikher, and F. Nori, Phys. Rep. **503**, 77 (2011).

¹⁷ A. Rozhkov, A. Sboyachkov, A. Rakhmanov, and F. Nori, Phys. Rep. **648**, 1 (2016).

¹⁸ A. Dyrdal and J. Barnas, Solid State Commun. **188**, 27 (2014).

- ¹⁹ Y.-F. Hsu and G.-Y. Guo, Phys. Rev. B **82**, 165404 (2010).
- ²⁰ A. O. Sboychakov, A. L. Rakhmanov, A. V. Rozhkov, and F. Nori, Phys. Rev. B **87**, 121401 (2013).
- ²¹ C. J. Tabert and E. J. Nicol, Phys. Rev. B **86**, 075439 (2012).
- ²² D. Wang and G. Jin, J. Appl. Phys. **114**, 233701 (2013).
- ²³ M. Sanderson, Y. S. Ang, and C. Zhang, Phys. Rev. B **88**, 245404 (2013).
- ²⁴ S. A. Owerre, J. Phys.: Condens. Matter **28**, 47LT02 (2016).
- ²⁵ Y. Yao, F. Ye, X.-L. Qi, S.-C. Zhang, and Z. Fang, Phys. Rev. B **75**, 041401 (2007).
- ²⁶ D. Wang and G. Jin, Phys. Lett. A **377**, 2901 (2013).
- ²⁷ J. B. Oostinga, H. B. Heersche, X. Liu, A. F. Morpurgo, and L. M. K. Vandersypen, Nat. Mater. **7**, 151 (2007).
- ²⁸ S. Y. Zhou, G.-H. Gweon, A. V. Fedorov, P. N. First, W. A. de Heer, D.-H. Lee, F. Guinea, A. H. C. Neto, and A. Lanzara, Nat. Mater. **6**, 770 (2007).
- ²⁹ M. Ryu, P. Lee, J. Kim, H. Park, and J. Chung, Nanotechnology **27**, 31LT03 (2016).
- ³⁰ H. M. Abdullah, M. Van der Donck, H. Bahlouli, F. M. Peeters, and B. Van Duppen, Appl. Phys. Lett. **112**, 213101 (2018).
- ³¹ W.-X. Wang, L.-J. Yin, J.-B. Qiao, T. Cai, S.-Y. Li, R.-F. Dou, J.-C. Nie, X. Wu, and L. He, Phys. Rev. B **92**, 165420 (2015).
- ³² P. San-Jose, A. Gutiérrez-Rubio, M. Sturla, and F. Guinea, Phys. Rev. B **90**, 075428 (2014).
- ³³ M. Kindermann, B. Uchoa, and D. L. Miller, Phys. Rev. B **86**, 115415 (2012).
- ³⁴ J. C. W. Song, A. V. Shytov, and L. S. Levitov, Phys. Rev. Lett. **111**, 266801 (2013).
- ³⁵ J. Jung, A. M. DaSilva, A. H. MacDonald, and S. Adam, Nat. Commun. **6**, 6308 (2015).
- ³⁶ M. Nevius, M. Conrad, F. Wang, A. Celis, M. Nair, A. Taleb-Ibrahimi, A. Tejeda, and E. Conrad, Phys. Rev. Lett. **115**, 136802 (2015).
- ³⁷ M. Zarenia, O. Leenaerts, B. Partoens, and F. M. Peeters, Phys. Rev. B **86**, 085451 (2012).
- ³⁸ B. Uchoa, V. N. Kotov, and M. Kindermann, Phys. Rev. B **91**, 121412(R) (2015).
- ³⁹ X. Zhai and G. Jin, Phys. Rev. B **93**, 205427 (2016).
- ⁴⁰ E. Prada, P. San-Jose, L. Brey, and H. Fertig, Solid State Commun. **151**, 1075 (2011).
- ⁴¹ F. Zhang, J. Jung, G. A. Fiete, Q. Niu, and A. H. MacDonald, Phys. Rev. Lett. **106**, 156801 (2011).
- ⁴² I. Lobato and B. Partoens, Phys. Rev. B **83**, 165429 (2011).
- ⁴³ Z. Q. Li, E. A. Henriksen, Z. Jiang, Z. Hao, M. C. Martin, P. Kim, H. L. Stormer, and D. N. Basov, Phys. Rev. Lett. **102**, 037403 (2009).
- ⁴⁴ Y. Xu, X. Li, and J. Dong, Nanotechnology **21**, 065711 (2010).
- ⁴⁵ H. M. Abdullah, B. Van Duppen, M. Zarenia, H. Bahlouli, and F. M. Peeters, J. Phys.: Condens. Matter **29**, 425303 (2017).
- ⁴⁶ I. Snyman and C. W. J. Beenakker, Phys. Rev. B **75**, 045322 (2007).
- ⁴⁷ Y. Blanter and M. Büttiker, Phys. Rep. **336**, 1 (2000).
- ⁴⁸ I. Redouani and A. Jellal, Mater. Res. Express **3**, 065005 (2016).
- ⁴⁹ H. M. Abdullah and H. Bahlouli, Journal of Computational Science **26**, 135 (2018).
- ⁵⁰ B. Van Duppen and F. M. Peeters, Phys. Rev. B **87**, 205427 (2013).
- ⁵¹ N. Gu, M. Rudner, and L. Levitov, Phys. Rev. Lett. **107**, 156603 (2011).
- ⁵² J. M. Pereira, F. M. Peeters, A. Chaves, and G. A. Farias, Semicond. Sci. Technol. **25**, 033002 (2010).
- ⁵³ M. Barbier, P. Vasilopoulos, F. M. Peeters, and J. M. Pereira, Phys. Rev. B **79**, 155402 (2009).
- ⁵⁴ D. R. da Costa, A. Chaves, G. A. Farias, and F. M. Peeters, J. Phys.: Condens. Matter **29**, 215502 (2017).
- ⁵⁵ M. Barbier, P. Vasilopoulos, and F. M. Peeters, Phys. Rev. B **82**, 235408 (2010).
- ⁵⁶ H. M. Abdullah, A. E. Mouhafid, H. Bahlouli, and A. Jellal, Mater. Res. Express **4**, 025009 (2017).